Single-cell transcriptomic profiling of the whole colony of *Botrylloides diegensis*: Insights into tissue specialization and blastogenesis

Authors: Berivan Temiz[1], Michael Meier[1-2], and Megan J. Wilson[1*]

[1]Developmental Biology and Genomics Laboratory, Department of Anatomy, Otago School of Biomedical Sciences, University of Otago, P.O. Box 56, Dunedin 9054, New Zealand[1]

[2]Department of Pathology, University of Otago, Dunedin 9054, New Zealand[2]

*** Corresponding Author:** Megan J. Wilson

Mail: meganj.wilson@otago.ac.nz

Orcid IDs of the Authors

Berivan Temiz - https://orcid.org/0000-0002-0499-8301

Megan J. Wilson - https://orcid.org/0000-0003-3425-5071

Running title: Single-Cell Profiling of *B. diegensis* Colony

Key words: ascidian, progenitor, single-cell sequencing, *Botrylloides*

Summary statement: Single-cell RNA sequencing of *Botrylloides diegensis* revealed cellular heterogeneity, identified 29 major cell clusters, and provided insights into tissue specialization and blastogenesis.

Abstract

Botrylloides diegensis is a colonial ascidian that has been the focus of developmental, evolutionary, and regeneration research. In this study, we performed single-cell RNA sequencing (scRNA-seq) of an entire *B. diegensis* colony, including zooids, buds, and vascular tunics, to resolve cellular heterogeneity and identify cell and tissue markers. We identified 29 major cell clusters within the colony and used *in situ* hybridization to examine the spatial expression of cluster marker genes. Numerous tissue types were identified at the molecular level, including blood cells and zooid tissues such as the branchial epithelium, stomach, and endostyle. Distinct cluster markers were identified for specific regions of the stomach epithelium, highlighting the specialization of these regions and the strength of using scRNA-seq to explore their functionality. Cell trajectory projections highlighted the early appearance of progenitor clusters, whereas more differentiated zooid-related tissues appeared later in the developmental path. This study provides a valuable resource for understanding the development, tissue function, and regeneration of *B. diegensis.* This demonstrates the power of scRNA-seq to define cell types and tissues in complex colonial organisms.

Introduction

Single-cell RNA sequencing (scRNA-seq) can quantify the total transcriptome of individual cells in the tissue/organism of interest. This information can be used to classify, characterize, and distinguish each cell at the mRNA level, allowing for the identification of different cell types, developmental states, and trajectories. Many studies have mapped the transcriptomic composition of diverse animals, including invertebrates such as planaria, sponges, *Hydra*, and ascidian species. These studies are essential to understand how cell types differ from each other through the activation or repression of specific pathways; therefore, they can explain how cells

53 possess pluripotency, commit to becoming specific biological units, access categorical
54 morphology, and become a part of tissue during development or regeneration.
55
56 Colonial ascidians are sessile marine chordates (Fig. 1A), which can be categorized into three
57 main parts:1) zooids, buds, and budlets as the asexually developing body; 2) the vascular
58 network, including veins, blood cells, and vascular termini/ampullae; and 3) tunic, the
59 gelatinous matrix covering all colonies (Berrill, 1947a; Blanchoud et al., 2017) (Fig. 1B and
60 C). At least 11 blood cell types have been identified in the hemolymph and are grouped into
61 five cell types:1) undifferentiated cells, hemoblasts, and differentiating cells; 2) immunocytes,
62 hyaline amebocytes, macrophage-like cells, granular amebocytes, and morula cells; 3)
63 transport cells, compartment amebocytes, and compartment cells; 4) mast cell-like cells or
64 granular cells; and 5) storage cells, pigment cells, or nephrocytes(Blanchoud et al., 2017; Cima
65 et al., 2001; Hirose et al., 2003; Wright and Ermak, 1982). The zooid, as a filter-feeding
66 individual, consists of various anatomical structures, including the atrial epithelium, atrial
67 siphon, branchial epithelium, bud, endostyle, gonads, intestine, neural complex, peribranchial
68 sacs, pericardium, pyloric gland, stigmata, and the stomach (Fig. 1D and E) (Anselmi et al.,
69 2022; Berrill, 1947a; Blanchoud et al., 2017; Holland, 2016; Kawamura and Sunanaga, 2010).
70 During asexual reproduction and blastogenesis, a new zooid is produced by budding from the
71 atrial epithelium of the parental zooid (Berrill, 1947a; Manni and Burighel, 2006; Mukai et al.,
72 1978). This budding process, also known as blastogenesis or palleal budding, is
73 morphologically similar to whole-body regeneration (WBR) (Berrill, 1951; Rinkevich et al.,
74 2007). Thus, studying intact whole colonies will help capture the critical aspects of their
75 development, tissue function, and regeneration.
76

Several sc-RNA-seq studies have been performed with the solidary ascidian *Ciona intestinalis*, mainly during the embryonic stage, showing the conservation of developmental and functional programs in chordate evolution (Cao et al., 2019; Horie et al., 2018; Sharma et al., 2019; Zhang et al., 2020). *B. diegensis* is an emerging model for development, regeneration, and stem cell studies owing to its small genome size, short replenishment period, and excellent example of WBR (Blanchoud et al., 2018). Therefore, investigating the composition of mature colonies is crucial to understand the cell types and tissues of *B. diegensis*.

This study aimed to develop a protocol and resource for *B. diegensis* to identify cell and tissue markers. Single-cell transcriptomic profiling of a mature (blastogenic stage A) *B. diegensis* colony was performed. Consequently, several cell and tissue types were separated based on their unique gene expression profiles, and their spatial expression was validated using *in situ* hybridization.

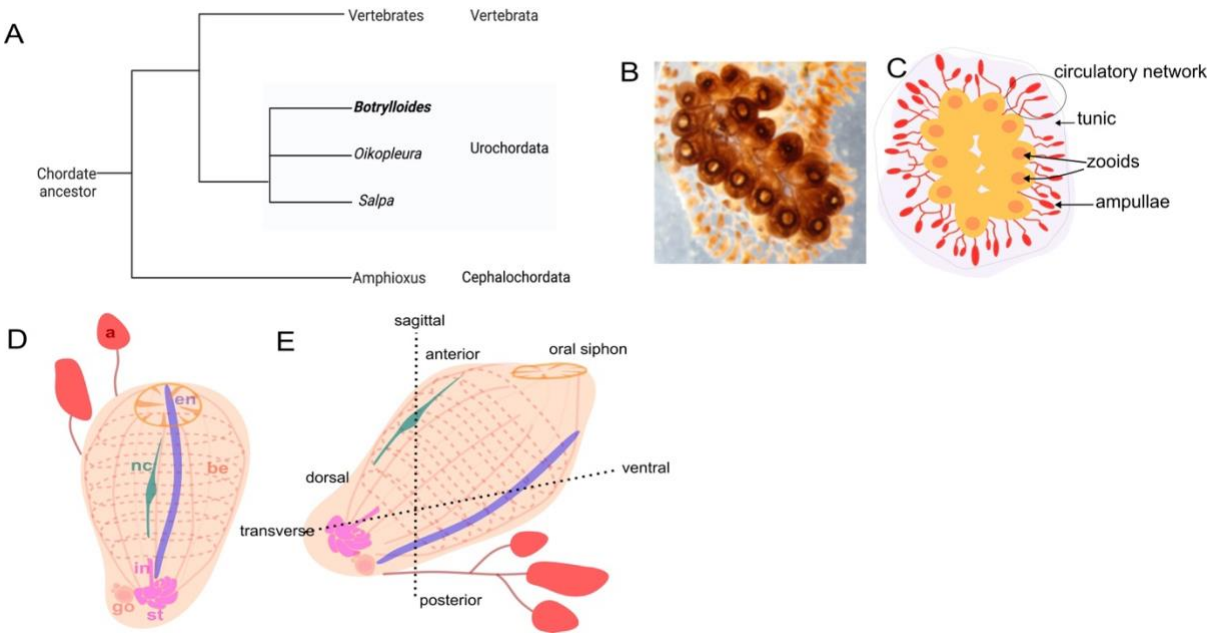

Figure 1. The study system: *Botryllodies diegensis.* A. Simplified phylogeny represents the position of tunicates as the closest chordate group to vertebrates. B. Example *B. diegensis* colony attached to a glass slide. C. Orange morphs of *the B. diegensis* colony are illustrated. The red lines indicate shared circulatory networks. The vascular termini (ampulla) are elliptical vascular ends. The individuals (zooids) are lined side by side in a ladder-like arrangement in the gelatinous matrix (tunic). D and E.

Simplified zooid anatomy, dorsal (D) and lateral (E) views. Abbreviations: intestine (in), stomach (st), gonad (go), neural complex (nc), endostyle (en), branchial epithelium (be).

Results and Discussion

B. diegensis colonies were obtained from a local marina and kept in the laboratory. We performed scRNA-seq using acetic acid-methanol (ACME) tissue dissociation and fixation methods (Fig. 2A). Cells from a *B. diegensis* colony at stage A of the blastogenic cycle were fixed and dissociated using ACME (Fig S1 A-B). This was followed by FACS sorting to remove cell aggregates and debris (Fig.S1E-L). Chromium^{TM} Single-cell 3' (10X Genomics) was used for single-cell barcoding. The barcoded reads were sequenced in both directions for paired-end sequencing. Library quality control was performed using FastQC software (Fig. S2). High-quality reads were mapped back to the reference genome using STARSolo software. The summary statistics for mapping are provided in Table S1. A single-cell transcriptome library containing approximately 58 million reads was generated. The percentage of the aligned reads with valid barcodes was 96%. The rate of reads that mapped to unique genes was 73%. In total, 6353 cells were detected, with a mean of 1586 UMIs and 481 genes per cell. A total of 13621 genes were identified (Table S1).

Cluster analysis was performed to group single-cell transcriptomes based on similarity using the Seurat software. Genes showing high variation between cells were calculated to obtain the best signal in cluster differences, and 2,000 genes were included by default. Twenty-nine distinct clusters were identified using nonlinear dimensional reduction with Uniform Manifold Approximation and Projection (UMAP) (Fig 2B). The cell numbers for each cluster are shown in Fig. S3. The highest cell number was observed for cluster 0, with 779 cells, and the lowest cell number was 25 for cluster 28. The mean cell number/cluster ratio was 208. The average number of genes in each cluster was 291.

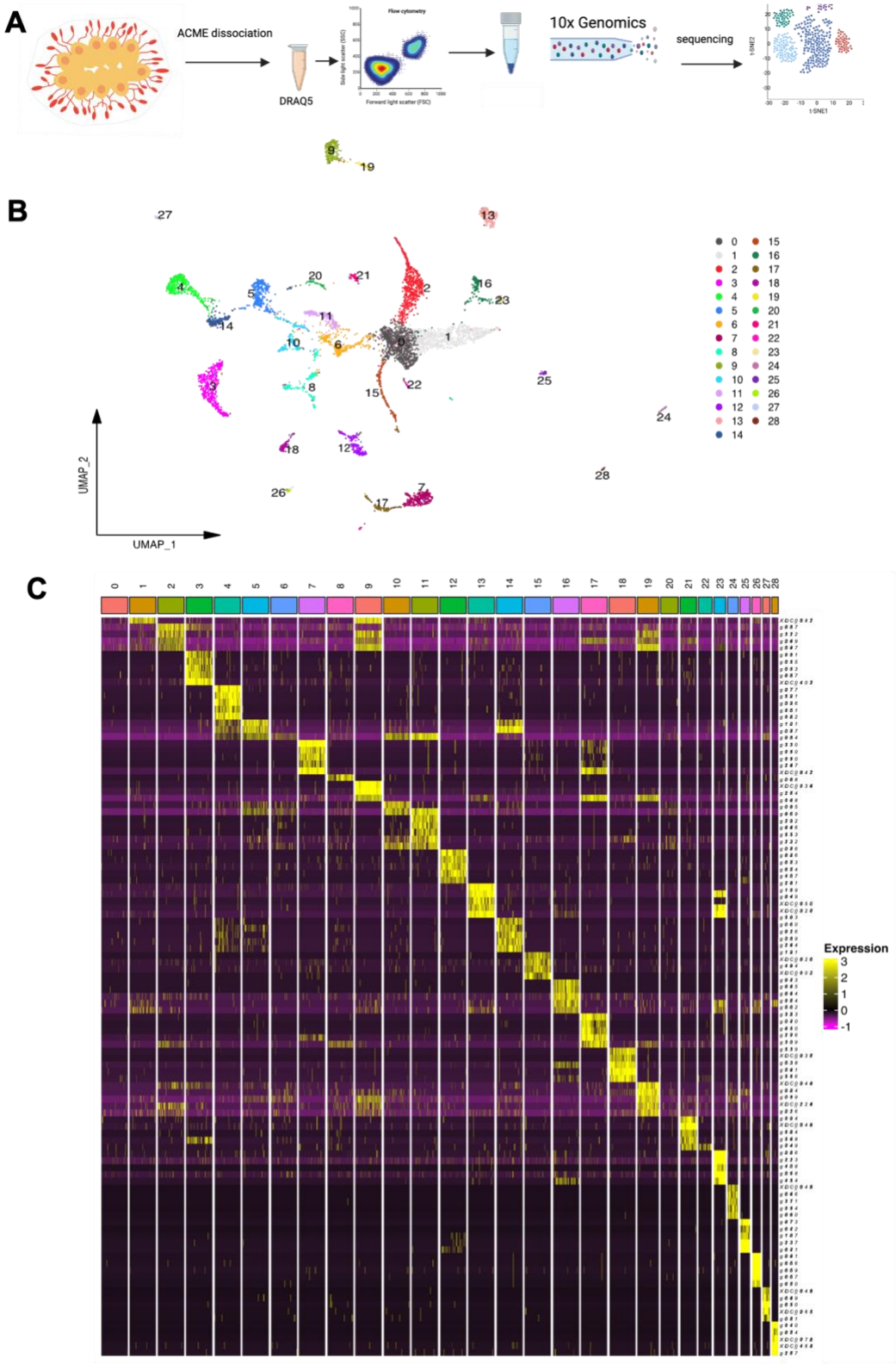

Figure 2. Overview of the experimental pipeline and clustering results. A. Single cells were prepared using the ACME maceration method (Garcia-Castro et al., 2021). Cells were stained with DRAQ5 and DRAQ5+ cells were sorted by FACS. Cells were captured in droplets using a 10X chromium system. Single-cell libraries were prepared and sequenced. After mapping the transcripts to the genome, clustering analysis was performed to

identify the cell types. B. UMAP clustering analysis revealed 29 single-cell clusters. Each cluster was color-coded. C. Heatmap of the top five marker genes in each cluster. Abbreviations: acetic-methanol (ACME).

Identification of Cluster Marker Genes

The FindMarkers function was used for differential expression analysis within the Seurat package to identify the top genes that were potential markers for each cluster (Fig. 2C). Differentially expressed genes (DEGs) were recorded as fold changes (LFC). The full DEG list for each cluster is provided in File S1. DEGs were annotated to their closest human orthologs. Genes that did not have vertebrate or human matches were also calculated for each cluster (Table S2). Gene ontology (GO) analysis was conducted for each cluster to aid the functional characterization of the clusters. The closest vertebrate orthologs that matched the DEGs were used to generate gene lists for GO analysis (File S2).

Using single-cell data to identify regional tissue markers

The expression patterns of the top marker genes of Clusters 4, 5, and 14 were determined by *in situ* hybridization (Fig. 3). *Ctrb1* (*g03753*) was one of the most highly expressed transcripts (~8 LFC) in Cluster 4, which was exclusively present in this cluster compared to other clusters (Fig 3A). *Ctrb1* encodes a serine protease enzyme linked to the acinar-like exocrine glandular cells involved in digestion (Perillo et al., 2016). A probe was designed to determine the cell-type expression of *Ctrb1,* and a strong staining signal was detected in the stomach of the zooid (Fig 3A). These *Ctrb1*+ epithelial cells were a subset of cells located in the outer curling of the stomach folds (Fig. 3A). No staining was observed in other tissues or vascular cells in mature colonies (Fig. 3A).

Kng1 (g08491) was identified as a marker for Cluster 14 (File S1) and was present to a lesser extent in Clusters 2, 4, and 5. A 610 bp fragment of *Kng1* was cloned and sequenced for use during *in situ* hybridization. Intense *Kng1* staining was observed within the lateral edges of the

stomach via *in situ* hybridization in adult tissue sections (Fig 3B). Thus, Cluster 14 was identified as a part of the stomach epithelium.

Cluster 10 marker g14532, a cornifelin-like gene (*Cnfn)*), showed specific expression in stigmata cells (Fig. 3C). This gene is localized to microtubules in humans, particularly in the epidermis and oral mucosa (Wagner et al., 2019), and is associated with cell-cell adhesion. It contains a cysteine-rich domain known as a PLAC8 domain.

Tubb was broadly upregulated in branchial epithelial tissues of the digestive tract (Fig. 3D). Tubb is a tubulin beta protein that functions in the microtubules of the cytoskeleton, controlling cell shape, movement, and transport within the cell (Sewell et al., 2024). Cilia are microtubule-based organelles, and the zone 1 cilium has a different axonemal structure than the other zones (*Ciona* endostyle) (Konno and Inaba, 2020), which may indicate that these cells express distinct combinations of microtubule genes.

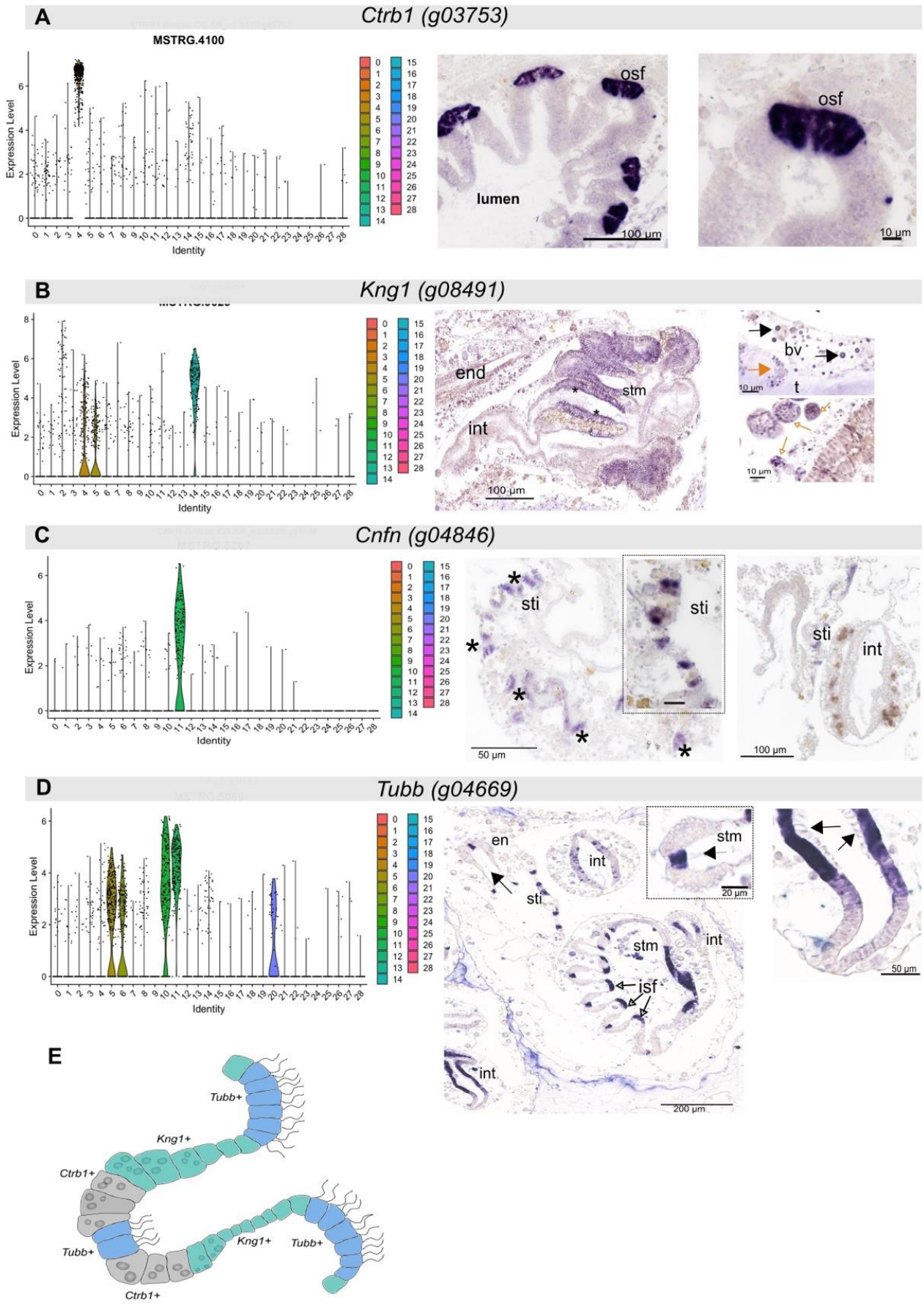
A
Ctrb1 (g03753)
MSTRG.4100
Expression Level
Identity
osf
lumen
100 µm
osf
10 µm
B
Kng1 (g08491)
Expression Level
Identity
end
stm
int
100 µm
bv
t
10 µm
10 µm
C
Cnfn (g04846)
Expression Level
Identity
sti
sti
50 µm
sti
int
100 µm
D
Tubb (g04669)
Expression Level
Identity
en
int
sti
stm
20 µm
stm
int
isf
int
200 µm
50 µm
E
Tubb+
Kng1+
Ctrb1+
Tubb+
Kng1+
Tubb+
Ctrb1+

Figure 3. Identification of *B. diegensis* digestive tract clusters. A. Violin plot showing *Ctrb1* as a marker of cluster 4. *In situ* expression of *Ctrb1* mRNA was observed in the cells on the outer side of each stomach fold. B. *Kng1*+ cells longitudinal stomach folds. C. Single-cell cluster expression profile for *Cnfn*, g04846, the top marker gene for Cluster 11. The *Cnfn* probe-stained cells are found in rows (asterixis) that line the branchial chamber, known as stigmata cells. D. Cluster expression for *Tubb* was identified as a top marker gene for Clusters 10 and 11, although it was expressed by cells found in several other Clusters. *Tubb* mRNA was found in the stomach epithelium, branchial epithelial cells, and epithelia covering the oocytes/eggs of developing buds. E. Based on the *in situ* results, an Illustration of a stomach fold showing the location of *Tubb+, Ctrb1*+ and *Kng1*+ cells in the stomach epithelium. Abbreviations: endostyle (end), stomach (stm), inner stomach fold (isf), outer stomach fold (osf), stigmata (sti), tunic (t), intestine (int).

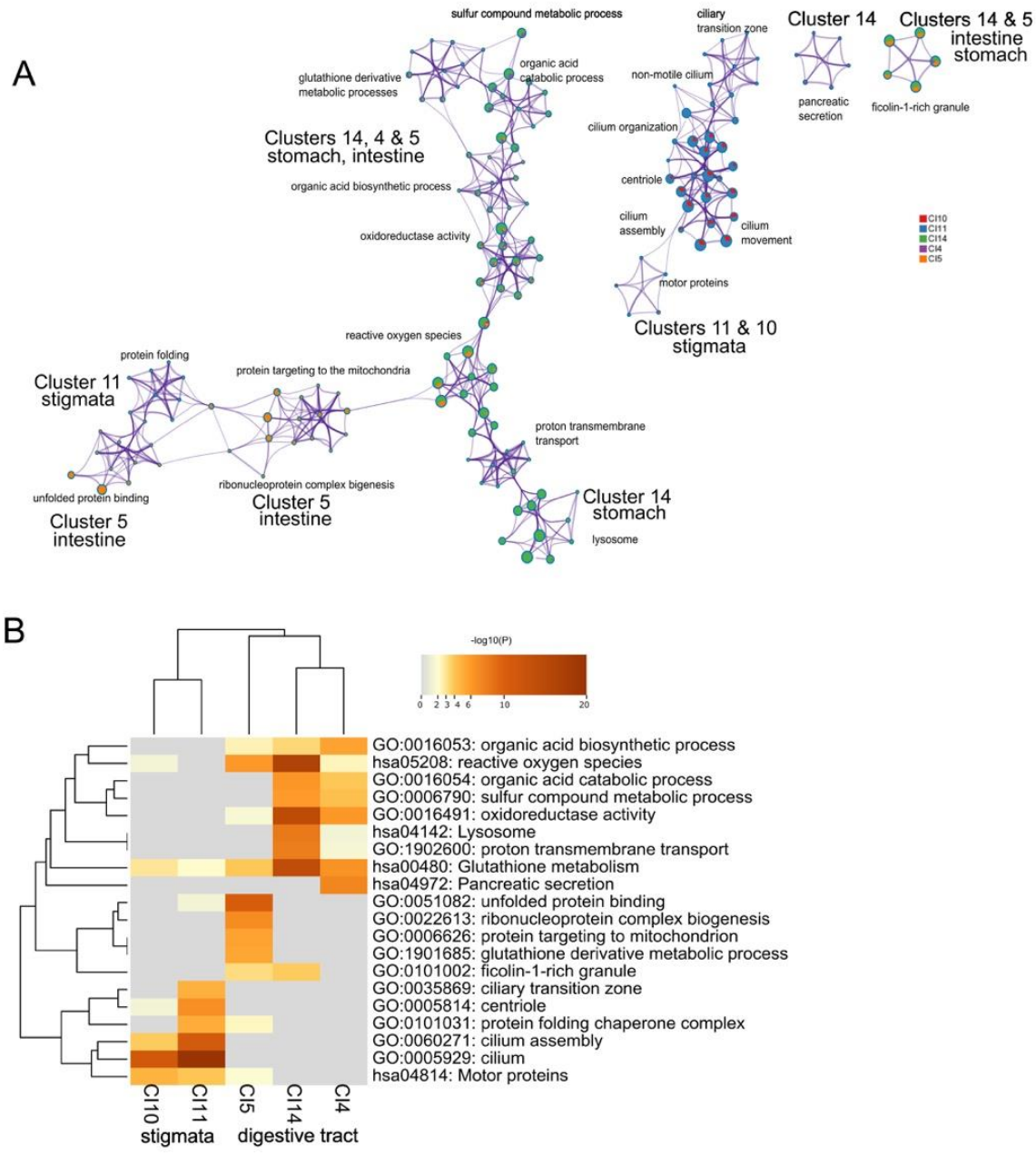

Figure 4. GO and pathway analyses for cell Clusters associated with digestive functions. A. Metascape network of enriched terms, colored by Cluster number and predicted tissue type. Each node is colored according

183 to the number of genes (from each list) associated with that term. B. A clustered heatmap of the top enriched GO
184 terms colored by p-values. Each row represents an enriched GO term, and each column represents the gene list
185 for Clusters 14, 4, 5, 10 and 11.
186

187 GO and pathway analyses were conducted for genes highly expressed in digestive- and
188 branchial-associated tissues (Clusters 4, 5, 10, 11, and 14) (Fig. 4). Clusters 10 and 11 were
189 overrepresented in the pathways linked to cilia assembly and movement (Fig. 4). This aligns
190 with the mRNA expression of *Cnfn* and *Tubb,* markers of cell clusters 11 and 10, respectively,
191 which showed intense staining in cilia-rich cell types (Fig. 3C and D). Annotation of clusters
192 4, 14, and 5 confirmed the enrichment of biological processes associated with food breakdown,
193 such as metabolic and catabolic oxidoreductase activity and cell secretion (Fig. 4).
194

195 **Identification of Endostyle clusters**

196 Endostyle, a tissue similar to the pharynx, filters food, synthesizes hormones, and provides
197 immune defences (Takagi et al., 2022). They are also believed to possess stem cell niches or
198 hematopoietic properties (Voskoboynik et al., 2008b). Genes known to be expressed in the
199 endostyle of other ascidian species (*Ciona, Styela*, and *Botryllus*) were selected and identified
200 using the single-cell dataset (Table S4). Clusters 6, 3, and 8 were deemed potential endostyle
201 clusters based on the expression of known endostyle markers. In the ascidian *Ciona*, galectin
202 is expressed in various regions of the endostyle (Parrinello et al., 2015; Parrinello et al., 2017).
203 The *B. diegensis* genome contains multiple *Lgal* genes (File S3) whose transcripts were
204 detected in clusters 3, 4, and 10 (File S3) (Fig. 5A). In *Styela*, *Itnl1/Fcn1* mRNAs were enriched
205 in clusters 8 and 3 and zones 6 and 7 of the endostyle (Jiang et al., 2023). *Muc5a* and *VWF*
206 transcripts were found in Clusters 3 and 10(Sasaki et al., 2003; Yamagishi et al., 2022).
207 Glutathione peroxidase, a common endostyle and branchial sac enzyme (Kobayashi et al.,
208 1983), was observed in our dataset in Clusters 3 and 6 (Fig. 5A).
209

GO and pathway analyses for Cluster 3 associated genes revealed enrichment for processes such as immunity, ECM, carbohydrate binding, and cell adhesion (Fig 5B). Jiang et al. (2023) also found a list of similar GO terms including ribosomal, thyroid hormone, immune function, digestive function (such as mucus), and neurosecretory genes (such as semaphorin 1a) for *Styela clava* (Jiang et al., 2023).

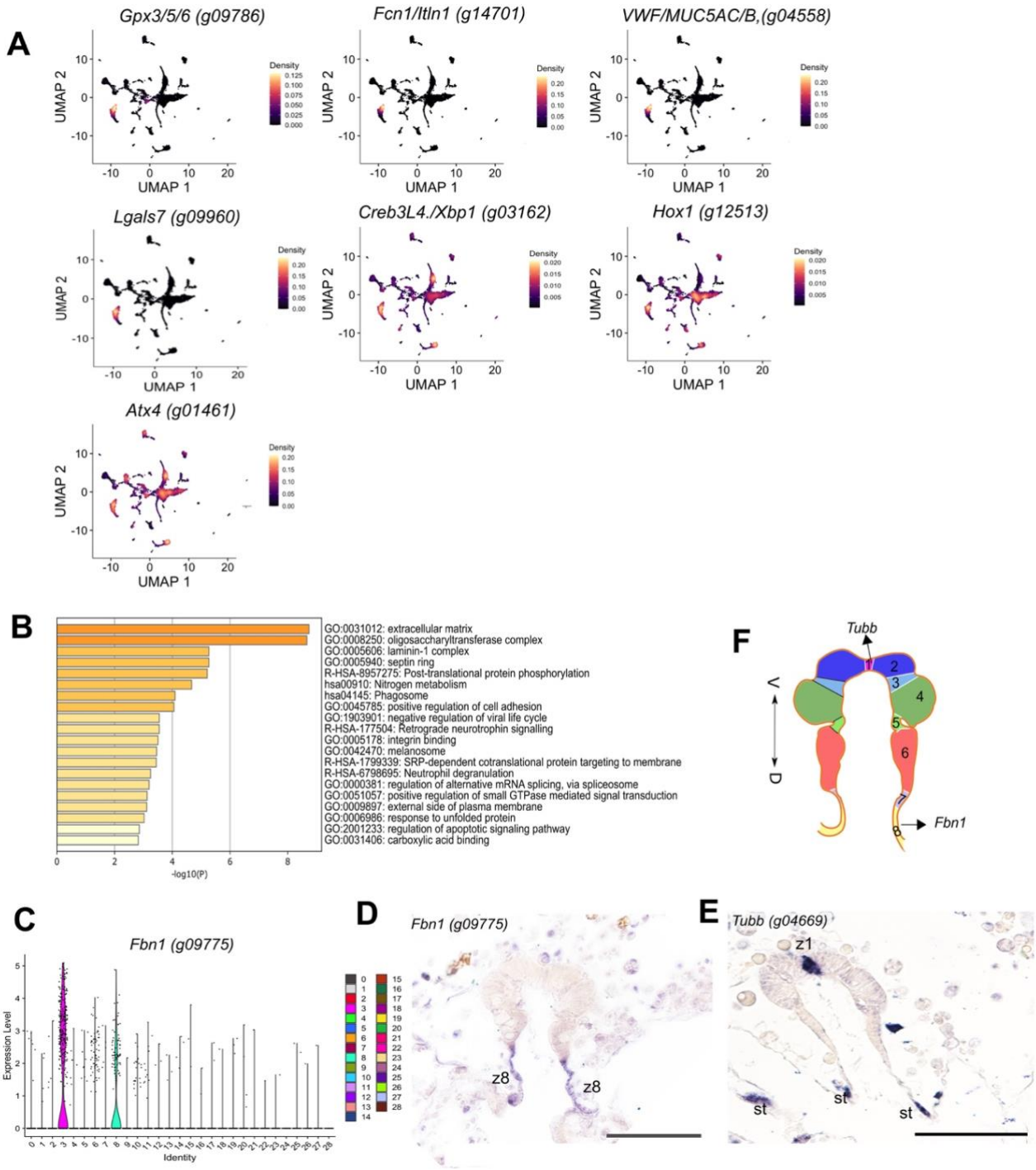

216

217 **Figure 5. Identification of Endostyle Clusters**. A. UMAP feature density plots showing the highest
218 concentration of cells expressing each of these tunicate endostyle genes. B. GO and pathway terms colored by p-
219 value as determined by Metascape. C. UMAP plot for cluster marker 3, *Fbn1*. D. *In situ* expression pattern for
220 Cluster 3 marker *Fbn1*, in zone 8 of the endostyle. E. *Tubb* mRNA was detected in zone 1 cells of the endostyle.
221 F. Schematic showing the different zones of the endostyle, highlighting the spatial expression of *Fbn1* and *Tubb*.
222 Abbreviations: zone 8 (z8), zone 1 (z1), stigmata (st), ventral (v), dorsal (d). Scale bar is 50 µm.
223

224 The top marker gene for Cluster 3, g09775, (Fig. 5C) encodes fibrillin (Fbn1), a protein with
225 fibrillin repeats and an EGF domain that shares 44% identity with the Human Fbn1/2/3
226 proteins. Fbn proteins are found in connective tissues and maintain the elasticity of the tissues.
227 It is critical for microfibril synthesis, as it binds to calcium and regulates TGF-β release,
228 growth, and development (Chaudhry et al., 2007; Handford, 2000; Reinhardt et al., 1996). *Fbn1*
229 expression was observed in zone 8 of the endostyle (Fig. 5D). This region of the endostyle
230 functions with zone 7 in immune activities, with high iodine and peroxidase activities (Jiang et
231 al., 2023; Sasaki et al., 2003) (Alesci et al., 2022). Iodine metabolism has been linked to thyroid
232 gland evolution (Fujita and Nanba, 1971). We also found that the *Tubb* probe (identified as a
233 ciliated cell marker in Fig. 3D) marked a subset of endostyle cells. *In situ* hybridization showed
234 that its mRNA was present in zone 1 cells of the endostyle (Fig. 5E). These cells have long
235 cilia, which together with mucus, aid in trapping food particles from the water current (Holley,
236 1986). Based on this information, Cluster 3 was assigned as an endostyle cell cluster.
237

238 **Identification of Blood cell clusters**

239 The top Cluster 25 gene g07537 is predicted to encode a FAD-dependent oxidoreductase
240 domain-containing protein (Foxred2) (Didion et al., 2002). This transcript was also detected in
241 some of the cluster 12 cells (Fig. 6A). Foxred2 functions to balance redox states and contributes
242 to the generation of reactive oxygen species (ROS), which are associated with endoplasmic
243 reticulum (ER) stress. Strong Foxred2 staining was observed in the thin endothelium lining

244 blood vessels and in a small number of immunocytes with a few large granules (Fig. 6A).
245 Additionally, staining was observed in the developing heart tube cells as they became thinner.
246 In ascidians, the expression of Foxred2-like proteins in the vascular lining and granular
247 immunocytes suggests that it may be crucial for maintaining redox balance and metabolic
248 processes critical for vascular function and immune response. This may include protecting cells
249 from oxidative stress, aiding in antimicrobial defence, detoxifying harmful substances, and
250 regulating inflammation. GO analysis (Fig. S10) revealed associations with heme binding,
251 biosynthesis, oxidoreductase activity, and SLC-mediated transmembrane transport within
252 Cluster 25. SLC-mediated transport is important for thin-monolayer barriers, such as the blood-
253 brain barrier, to mediate the transport of substances across the endothelium (Morris et al.,
254 2017).
255
256 The expression of the Cluster 13 marker, Glutathione S-Transferase Alpha 3 (*Gst3A*) *g11109,*
257 was also detected in some cells and distributed throughout the other clusters (Fig 6B).
258 Staining was observed in cytotoxic cells, including granular amoebocytes (Fig.6B, asterisks),
259 compartment amoebocytes, and morula-like cells (Fig. 6B). Morula cells are variable in size,
260 and the extent of staining may have been influenced by vacuole size. Only a few significantly
261 enriched GO terms were identified because of the low number of marker genes in this cluster.
262 However, it included immune system processes (Fig. S10).
263
264

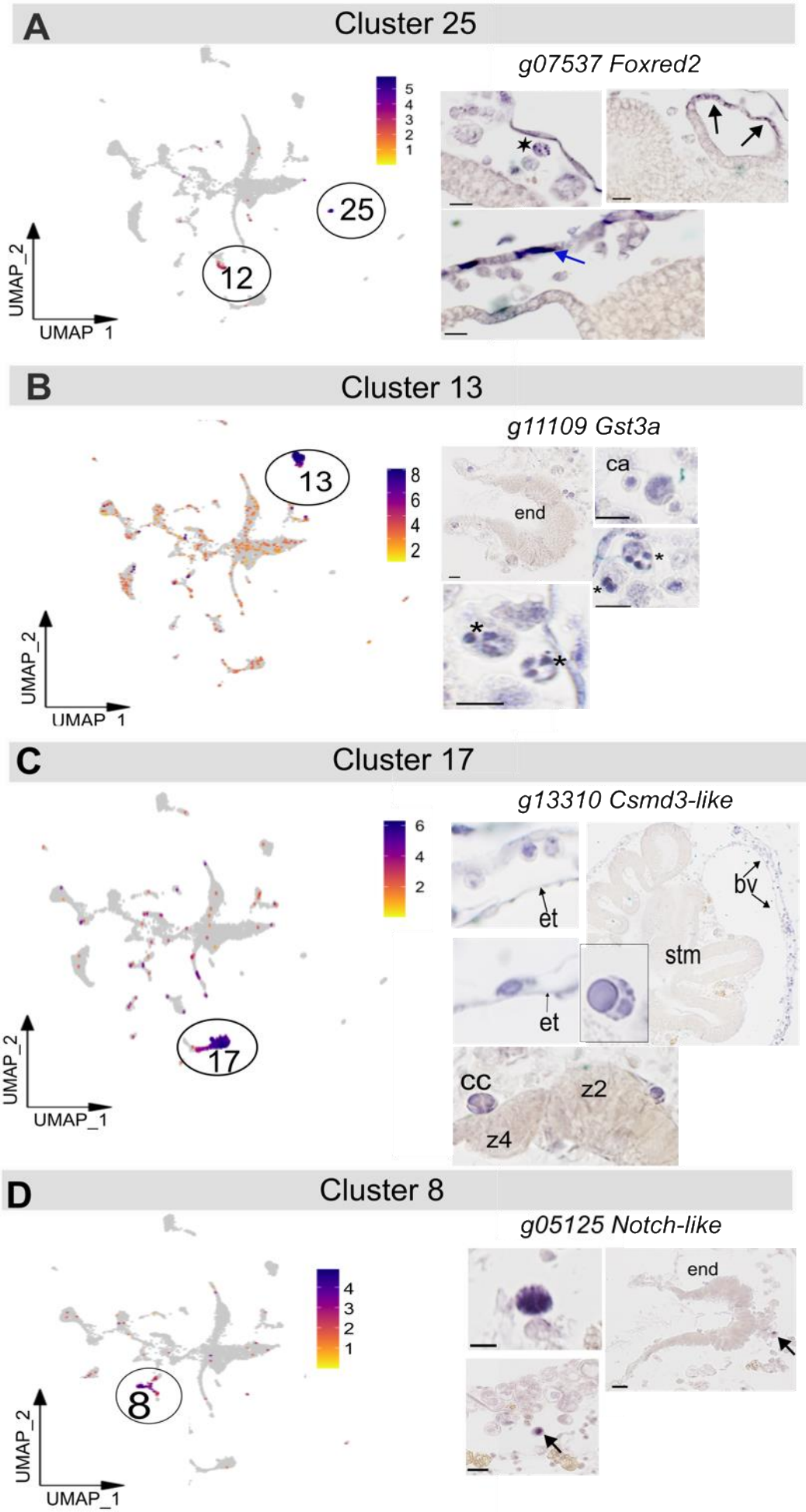
A
Cluster 25
g07537 Foxred2
5
4
3
2
1
25
12
UMAP_2
UMAP_1
B
Cluster 13
g11109 Gst3a
13
8
6
4
2
end
ca
UMAP_2
UMAP_1
C
Cluster 17
g13310 Csmd3-like
6
4
2
et
bv
stm
et
17
cc
z2
z4
UMAP_2
UMAP_1
D
Cluster 8
g05125 Notch-like
4
3
2
1
end
8
UMAP_2
UMAP_1

Figure 6. Candidate blood cell clusters. A. UMAP feature plot for Cluster 25 marker, *Foxred2*. Detection of Foxred2 mRNA by in situ hybridisation identified vascular endothelium (blue arrow), cells of the developing heart and some blood cells (asterisk). B. Cluster 13, g11109 *Gst3a*. C. Cluster 17 marker, g13310 (*Csmd3*). *In situ* hybridization with *Csmd3,* with mRNA-positive vesicles indicated (asterisks). D. Cluster 8 marker *g05125* (*Notch-like*). Only a few scattered cells in the vascular stained with the *g05125* probe (arrows). Abbreviations: stomach (stm), vessel endothelium (et), blood vessel (bv), endostyle (end), compartment amoebocyte (ca), compartment cell (cc), zone 2 (z2), zone 4 (z4) The scale bars are 10 μm.

The gene g13310 was identified as a cell marker for Cluster 7 (Fig. 6C). This gene is predicted to encode a protein ortholog of CSMD3 with multiple Sushi and von Willebrand factor type A (CUB) domains, typically found in transmembrane receptors or adhesion proteins. Sushi or complement control domains are involved in the immune system (Ermis Akyuz and Bell, 2022). Excessive activation of the complement pathway is prevented by Sushi domain-containing proteins, which bind to activated C3/4 components to target them for degradation (Ojha et al., 2019). *Csmd3*+ cells were detected in the circulation (Fig. 6C), which appeared to be phagocytic cells, including macrophage-like cells and hyaline amoebocytes. Gene ontology analysis revealed an overrepresentation of terms related to the cytoskeleton, apoptosis, and immunity (Fig. S9).

Cluster 8 top marker gene, *g05125* (Fig. 6D), codes for a large protein that shares 30% identity with NOTCH1, NOTCH2, and SNED1 due to multiple Sushi and EGF domains. Several Notch-like genes are present in the *B. diegensis* genome. *In situ* hybridization detected expression in a small number of storage and/or granular cells; larger cells were characterized by multiple small vesicles (Fig. 6D). These cells resemble mast cells and are predicted to release inflammatory factors such as histamine and chemokines (Blanchoud et al., 2017; Cima et al., 2001). Gene Ontology and pathway analysis indicated terms related to peroxidase and leukocyte-mediated immunity (Fig. S11).

Developmental Trajectory analysis

295 To identify the cells forming the bud disc of the peribranchial epithelium, we examined cells
296 with thickened epithelium (Berrill, 1947b) and budlet/vesicle precursors. We focused on
297 identifying the cells with the highest expression of transcription factors found in disc cells,
298 *Pitx1, Otx, Nk4*, and *Runx* (Langenbacher et al., 2015; Ricci et al., 2016; Tiozzo et al., 2005).
299 The subset of cells within Cluster 6, likely the peribranchial cluster, showed the highest joint
300 density, indicating that cells co-expressed these four genes (Fig. 7C). Using this as the root, the
301 predicted cell trajectory was plotted using the Monocle3. Pseudotime trajectory paths indicate
302 the progression and pathways of these cells, going from this putative stem cell cluster to more
303 differentiated states later in the pseudotime. This analysis connected all Seurat clusters, with
304 the origin located in Cluster 6 (Fig. 7C). To extend this further, we determined whether several
305 previously studied candidate stem cell markers were present in the scRNA-seq dataset,
306 including *Itga6*, *Notch2*, *Vasa*, and *Piwi* (Kassmer et al., 2020; Kawamura and Sunanaga, 2010;
307 Rinkevich et al., 2010; Rosental et al., 2018). *Vasa, Piwi1*, and *Piwi2* were missing from the
308 dataset. *Notch2* and *Itga6* were detected in the cells scattered across several clusters (Fig. S12).
309 The proportion of dense cells was the same as that of bud disc genes (Fig. S12 and Fig. 7).
310 Additionally, orthologs of the reprogramming factors (Yamanaka factors) (Takahashi and
311 Yamanaka, 2006, 2016), *Oct3/4 (*POU3/4 proteins), *Sox2* (SOXB subgroup of Sox factors),
312 *Klf4*, and *cMyc* were found in the same group of cells within cluster 6 (Fig. S13). This further
313 supports the notion that a subset of Cluster 6 cells likely has stem cell properties and represents
314 the bud disc.
315

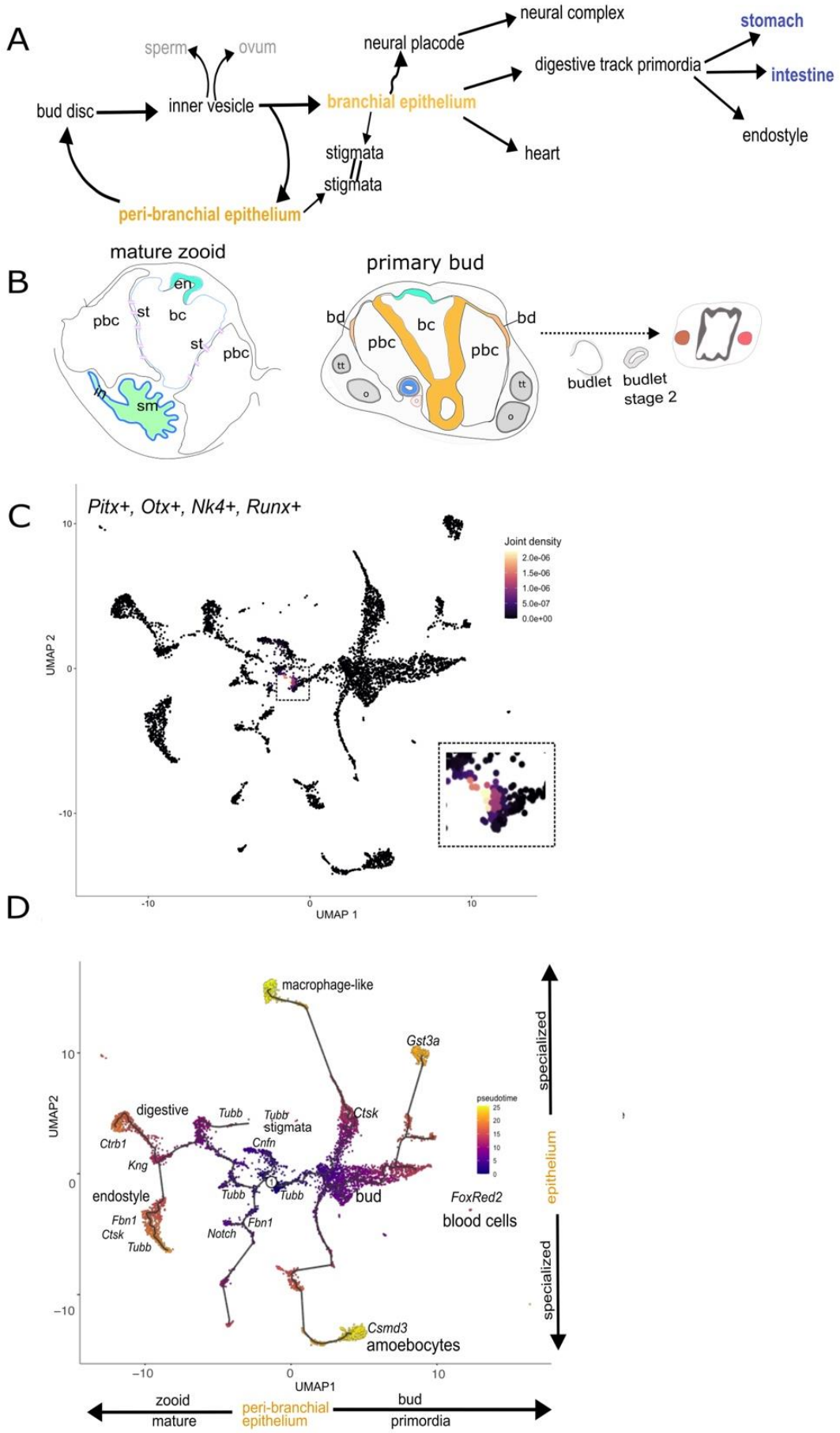
A
sperm
ovum
neural placode
neural complex
stomach
digestive track primordia
intestine
bud disc
inner vesicle
branchial epithelium
endostyle
stigmata
heart
stigmata
peri-branchial epithelium
B
mature zooid
en
pbc
st
bc
st
pbc
in
sm
primary bud
bd
bc
bd
pbc
pbc
tt
tt
o
o
budlet
budlet
stage 2
C
Pitx+, Otx+, Nk4+, Runx+
Joint density
2.0e-06
1.5e-06
1.0e-06
5.0e-07
0.0e+00
UMAP 2
UMAP 1
D
macrophage-like
Gst3a
specialized
digestive
Tubb
Tubb
stigmata
Ctsk
Ctrb1
Cnfn
Kng
pseudotime
endostyle
Tubb
Tubb
bud
FoxRed2
blood cells
epithelium
Fbn1
Ctsk
Tubb
Notch
Fbn1
specialized
Csmd3
amoebocytes
UMAP2
UMAP1
zooid
mature
peri-branchial
epithelium
bud
primordia

Figure 7. Cell populations and their relationships. A. Summary of the main tissue and organs formed. B. Example schema showing the relationships between tissues. The bud arises from a small group of cells (3-4 cells) within the epithelium of the peribranchial chambers, which appear in the immature zooid before the stigmata perforate. These cells form the bud disc. (Berrill, 1947). The disc separates from the epithelium to form a closed vesicle surrounded by the outer epidermis obtained from the parent zooid. Germ cells segregate early from the inner vesicle and form oocytes and sperm. On the dorsal side of the vesicle, the invagination forms a neural placode. The heart and digestive tracks form on the posterior side, and primordia form first as outpockets of the branchial epithelium. C. UMAP density plot showing co-expression of *Pitx, Otx, Nk4*, and *Runx* in cells located in Cluster 6. Cells with higher joint densities were more orange in color. D. Monocle 3 trajectory analysis. The root is the progenitor (within cluster 6, likely the peribranchial epithelium). Abbreviations: endostyle (en), stigmata (st), peribranchial chamber (pbc), branchial chamber (bc), intestine (in), stomach (sm), testes (tt), ovary (o), bud disc (bd).

The trajectory of the colony dataset was analyzed to understand the relationship between cell clusters and differentiation time using Monocle3 (Fig. 7D). The trajectory of cell development was charted on UMAP, with the candidate progenitor bud disc cells of the peribranchial cluster (Cluster 6) serving as the root (Fig. 7C). Pseudotime trajectories reveal that the clusters, predicted to be bud, peribranchial and brachial epithelial cells, emerge early. In contrast, clusters associated with specialized tissues, such as the stomach epithelium and neuronal clusters, were later in the pseudotime (Fig. 7D). Epithelial tissues within the zooid appeared early in the trajectory, preceding the development of stomach and endostyle tissues (left branch). The third pathway leads to immune cell formation. Overall, the development of zooid-related tissues later in the trajectory was consistent with blastogenesis (Fig. 7A and B)

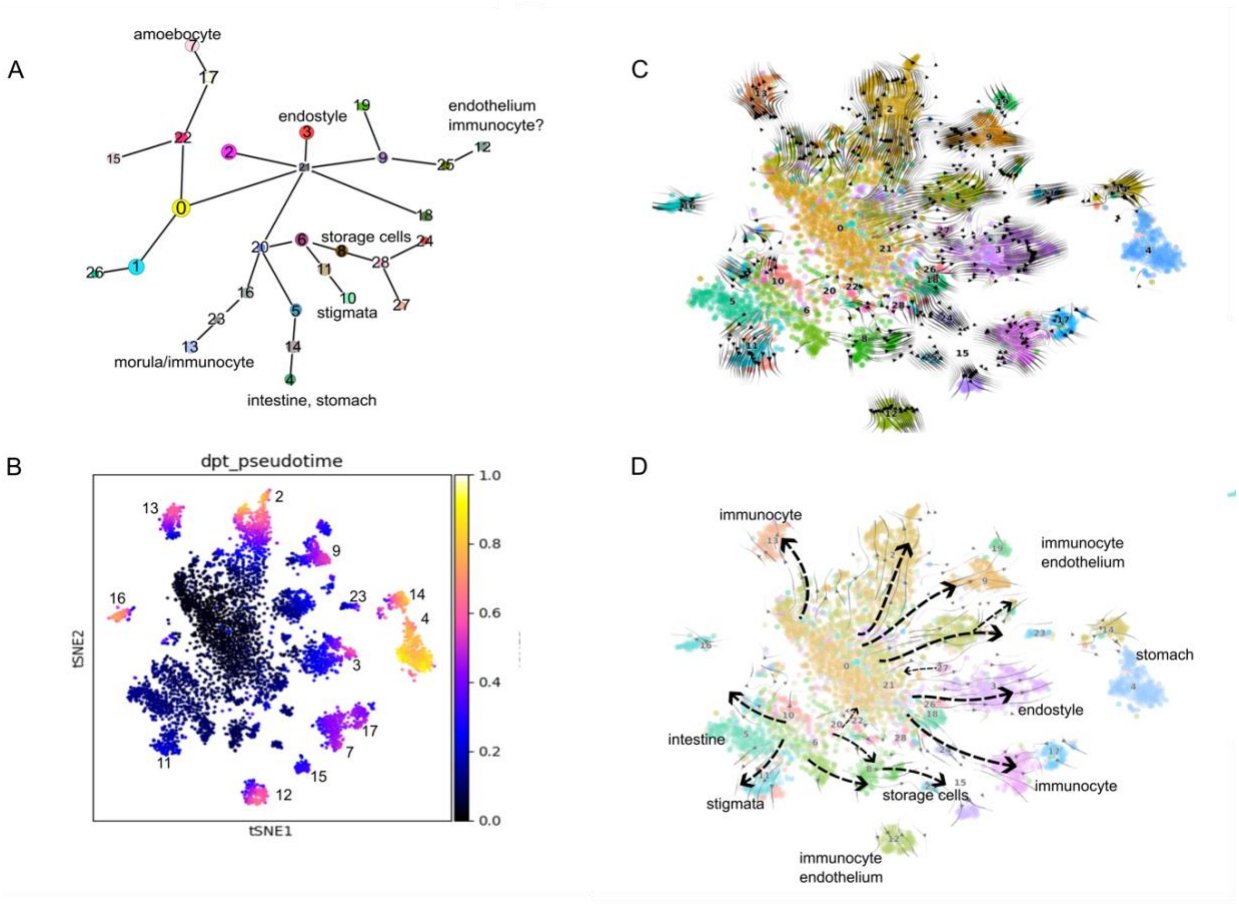

Figure 8. Identification of potential differentiation pathways using CellRank. A. The PAGA plot displays each cell cluster as a node, with branching lines indicating potential differentiation pathways among the clusters. B. A tSNE projection where cells are colored by pseudotime, showing the progression of cell states over time. Darker colors represent earlier pseudotime states, whereas lighter colors represent later pseudotime states. The Cluster IDs are given for the later states. A UMAP projeciont is shown in Fig. S15. C and D. Velocity plots using the tSNE projection, where arrows represent the direction of RNA velocity, indicating the predicted future states of the cells based on their transcriptional activity and pseudotime. The cells are colored using the Seurat Cluster ID. D. An annotated version of plot C shows detailed identification of specific cell types and their predicted differentiation pathways.

To explore the relationships between clusters, we generated PAGA plots to investigate the underlying structure and infer the potential differentiation pathways (Fig. 8A). This suggests that multiple common progenitor populations may give rise to differentiated cell types. The relationships between different clusters of cells during colony asexual reproduction were visualized, with each node representing a distinct cluster identity. Lines connecting the nodes illustrate lineage relationships between clusters. By examining central nodes with numerous connections, such as nodes 20, 21, 0, and 6, we can identify potential progenitor states that can

differentiate into several other states. These clusters had numerous outgoing edges, indicating potential branching points in the differentiation trajectories (Fig. 8A). Finally, the cell clusters at the ends of the branches represent the terminally differentiated states, and this largely matches the later cell Clusters identified in pseudotime analyses (Fig. 8C and 7D).

The velocity (scvelo) plot utilizes the spliced-to-unspliced mRNA ratio to indicate the direction of the cell transition. The length of the arrows in the velocity plot represents the speed of the transitions, with longer arrows indicating faster transitions and shorter arrows indicating slower or more stable transitions. This provides dynamic information about cellular processes. Additionally, the arrows converged at specific points, offering further insights into the directionality and progression of cell states. Clusters with numerous outgoing arrows are highlighted, emphasizing their roles in cellular differentiation (Fig. 8C). This plot was consistent with the PAGA plot, particularly with multiple transition events from clusters 0, 6, 21, and 20 (Fig. 8A), suggesting that cells within these clusters serve as central nodes with multiple connections (Fig. 8D).

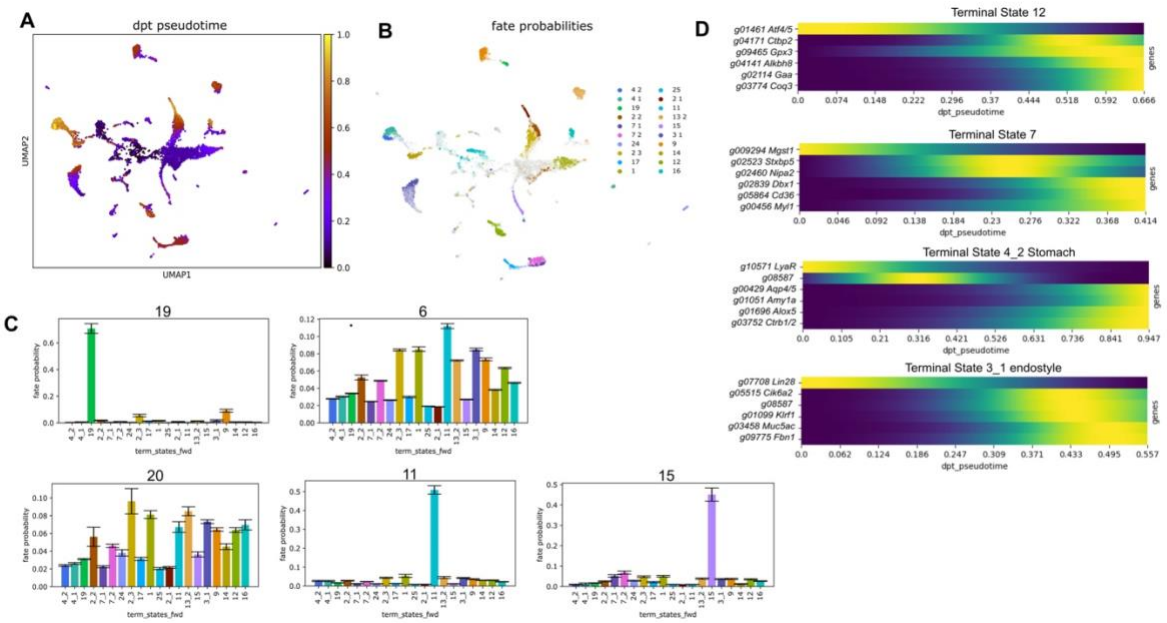

Fig. 9. Cell fate dynamics. A. UMAP plot showing diffusion pseudotime (dpt_pseudotime). The color scale represents pseudotime, cells colored yellow appear later in the predicted cell trajectory pathway. B. Fate

probability UMAP, shown as terminal clusters. C. Aggregate fate probabilities fate bar graphs. These display the probabilities of different clusters (22, 11, 15, 19, and 6) progressing towards the terminal states, as predicted by CellRank. D. A selection of driver genes is displayed alongside a gene whose expression is highest at the earliest pseudotime on the lineage towards the terminal state fate (File S4).

Finally, CellRank was used to examine the cell fate dynamics (Fig. 9). It has been designed to deal with complex data, such as data produced from developing and regeneration tissues, with many initial, intermediate, and terminal cell states (Lange et al., 2022). Figures 9C and S14 display a bar graph of the aggregate fate probabilities of cells from the Seurat cluster. These cells will progress to a terminal state, and the clusters with multiple bars of varying height have different probabilities of transitioning to different end states, such as Clusters 0, 5, 6, 8, 20, 18, 21, 22, 26, and 28. In contrast, clusters with cells that transition to one fate predominantly have a single high bar. For example, all cells in Cluster 11 transitioned to the ciliated stigmata cell type, according to GO and *in situ* expression (Fig. 3C).

We used CellRank to identify potential driver genes strongly associated with the terminal state that may serve as key regulators or markers of cell fate (Fig. 9E and File 4). These genes exhibited high expression levels at the earliest pseudotime but were low in the final terminal state. Such genes may play a role in initiating or driving the early stages of differentiation and then decreasing their expression as cells reach their final differentiated state. One example of a potential driver gene is the *Lin2*8 ortholog, a highly conserved RNA-binding protein that regulates stem cell differentiation and proliferation in organisms ranging from nematodes to mammals (Wu et al., 2022). This gene is expressed in undifferentiated pluripotent cells and is downregulated as cells progress toward a specialized cell fate or undergo reprogramming (Pieknell et al., 2022). Another potential driver gene was *the Atf4/*5 ortholog. In vertebrates, this transcription factor is associated with stress-induced responses and the differentiation of stem cells into secretory cells. It plays a role in epithelial differentiation and stresses immune

403 response (Barrera-Lopez et al. 2024). *B. diegensis g11626* encodes a DExD/H-box polypeptide,
404 39 B (DDx39b)-like RNA helicase. DDx39b regulates mRNA splicing events, including the
405 processing of transcripts of genes required for immune and myocyte cell fate (Hirano et al.,
406 2023; Zhang et al., 2018). Another potential driver gene is high mobility group box 1 (*Hmgb1*),
407 a chromatin-associated protein secreted by immune cells and involved in differentiating
408 mesenchymal stem cells into vascular cells (Meng et al., 2018).
409
410 Together, these analyses provided strong supporting evidence for the inferred differentiation
411 pathways. They identified key transitional cell clusters and several candidate progenitor cell
412 populations.
413
414 **Discussion**
415 Using sc-RNA-seq, we gained insights into the cellular content of a *B. diegensis* colony. This
416 technology identifies cluster markers by deconstructing the cellular heterogeneity of the filter-
417 feeding colony tissues. The colonial tissue was resolved into 29 clusters, including zooid and
418 vascular tissues. As a more ancestral chordate, *B. diegensis* occupies an essential phylogenetic
419 space with vertebrates, highlighting its significance in evolutionary and developmental
420 research. This sc-RNAseq resource paves the way for examining the cellular composition of
421 the colonial chordate, *B. diegensis*.
422
423 Based on the marker expression profiles that were highly and distinctively expressed in each
424 cluster, the colonial cellular profiles showed conserved gene regulatory programs and
425 functions. In contrast, clusters not enriched for a particular group of markers or functional
426 annotations may indicate an intermediate cell state. Although we found some blood cell
427 markers, some predicted hemocyte clusters showed intermediate and non-specific gene

428 expression patterns. These functions were not specifically enriched for the blood type because
429 of functional annotations based on the closest vertebrate relatives. Similarly, some blood
430 populations of *B. schlosseri* did not exhibit specific functions and contained unannotated genes
431 with invertebrate homologues (Rosental et al., 2018).
432
433 Trajectory analysis of cell fate during blastogenesis suggested that multiple initial and
434 intermediate states are present in the colony at any given time. In ascidians, bud development
435 is initiated by the emergence of bud primordium through the thickening of the peribranchial
436 epithelium via dedifferentiation or transdifferentiation (Manni et al., 2007). The peribranchial
437 epithelium corresponded to Cluster 6 in our study. Our gene expression analysis in Cluster 6
438 supports the hypothesis that the peribranchial epithelium is a critical source of progenitor cells
439 for bud development. The endostyle has been proposed as a stem cell niche in zooids,
440 suggesting a more transitional stem cell source for the colony (Voskoboynik et al., 2008a).
441 Specialized progenitors associated with the vascular lining and epithelial tissues have also been
442 identified. This demonstrates the ability of epithelial tissues to function as a source of
443 progenitors, preserving progenitor-like characteristics. This is significant because it indicates
444 that *Botrylloides* stem cells may not be fixed in one location, but can transition between
445 different niches within the organism. Additionally, the presence of transitional stem cell niches,
446 such as endostyle, highlights the dynamic nature of stem cell populations in these organisms.
447
448 Adult stem cells (ASCs) are involved in various epithelial tissues in invertebrates. For example,
449 in sponges, epithelial cells function similarly to stem cells and play a role in tissue repair
450 (Rinkevich et al., 2022). This observation suggests a conserved mechanism across different
451 invertebrate species where epithelial cells have multipotent capabilities essential for
452 regeneration and repair. This comparison underscores the importance of epithelial and vascular

453 progenitors in colonial ascidians and other invertebrates, indicating a potentially conserved
454 evolutionary strategy for tissue regeneration and maintenance. We hypothesized that epithelial-
455 and vascular-associated progenitors play key roles in the development and maintenance of
456 colonial ascidians.
457
458 Assigning cellular identities in scRNA-seq is inherently challenging because of the complexity
459 and variability of the gene expression profiles. The study was based on a limited set of
460 approximately 6,000 cells, which may not capture the full diversity of cell types in the
461 organism. Low-abundance transcripts may be underrepresented, leading to a potential bias in
462 gene expression data and overlooking genes expressed at low levels. Obtaining cells from the
463 tunic, which is rich in cellulose, presents a significant challenge, leading to the absence of
464 certain tunic cell types. The timing of colony collection might have missed some stages of the
465 sexual cycle, potentially omitting important cell types or developmental stages. For example,
466 the stages of oogenesis will be missed as *B. diegensis* only sexually reproduces briefly at the
467 end of the summer in New Zealand.
468
469 *In situ* hybridization, which is useful for the spatial localization of gene expression, is difficult
470 to quantify accurately, limiting its utility in confirming single-cell RNA sequencing (scRNA-
471 seq) findings. No one cluster was identified as marked by gene expression commonly attributed
472 to stem-like cells in colonial ascidians (Ballarin and Rosner, 2022). Specifically, previously
473 identified germline markers for colonial and solitary tunicates, such as *Piwi* or *Vasa*
474 (Kawamura et al., 2011; Rinkevich et al., 2010), were missing from the dataset. This absence
475 could be due to technical dropout, a common issue in scRNA-seq where lowly expressed genes
476 might not be detected in every cell, leading to their apparent absence in the data (Kharchenko
477 et al., 2014). The genes in *B. diegensis* were named and assigned functions for gene ontology

analysis based on their closest vertebrate orthologs, assuming similar functions in ascidians. However, many genes lack orthologs, making functional prediction more challenging.

SUMMARY

In this study, we performed single-cell RNA sequencing (scRNA-seq) on an entire *B. diegensis* colony, including zooids, buds, and the vascular tunic, to identify cell and tissue markers and resolve cellular heterogeneity. The analysis identified 29 major cell clusters within the colony, and *in situ* hybridization was used to examine the spatial expression of the cluster marker genes. Various tissue types have been identified at the molecular level, including blood cells and zooid tissues such as the branchial epithelium, stomach, and endostyle. Distinct cluster markers were found in specific regions of the stomach epithelium, highlighting their specialization. Trajectory estimations were aligned with predictions based on the early appearance of progenitor clusters, whereas zooid-related tissues appeared later in the developmental path. This study provides a valuable resource for understanding the development, function, and regeneration of *B. diegensis*, and demonstrates the power of scRNA-seq in defining cell types and tissues in complex colonial organisms.

Methods

Animal husbandry

Colonies of *B. diegensis* were sampled from Otago Harbor in New Zealand (45°52’18.1″”S, 170°31’37.6”″ E). The animals were attached to 5x7 cm glass slides. The tanks were aerated, and the colonies were fed a shellfish diet (a blend of marine microalgae). The colonies were fed every two days, and the seawater was replaced. Colonies were confirmed to be *B. diegensis* by COI barcoding (Temiz et al., 2023).

503 **Single-cell preparation & FACS**

504 Single cells of *B. diegensis* were prepared using the ACME dissociation method described by
505 García-Castro et al. (2021). Fresh ACME solution was prepared for fixation and separation of
506 tissue cells. It contained DNase/RNase-free distilled water, methanol, glacial acetic acid, and
507 glycerol at a ratio of 13:3:2:2. The mature colony was in stage A of blastogenesis with active
508 filtering, newly emerged primary buds, and no signs of secondary buds. The colony was placed
509 in a Petri dish on a glass slide, where it was attached using a microtome razor blade with
510 minimal disturbance. The animal was washed with 1 ml of 7.5% N-acetyl l-cysteine in 1XPBS.
511 This solution removes excess seawater and protects RNA. One mL ACME was added, and the
512 colony was minced well using a single-edged razor blade.

513

514 The suspension and all the larger tissue pieces were placed in a 1.5 mL tube. The tube was
515 placed in a rotator to apply seesaw motion at ~30-40 rpm for 1 h at room temperature. The
516 sample was pipetted twice and strained with a 40 µm cell strainer into an ice-covered 50 mL
517 Falcon tube. The cells were cooled to prevent RNA degradation. The suspension was
518 centrifuged at 1000 *g* for 5 min at 4°C. The supernatant was removed, and the pellet was
519 apparent. One mL of 1% BSA-1XPBS with RNase inhibitor was added to the pellet, and the
520 tube was flicked to mix. As the second washing step to remove all ACME, 1 mL of 1% BSA-
521 1XPBS with RNase inhibitor was added to the tube, and the tubes were flicked. A 70 µm
522 flowmi cell strainer was used to strain the cells to decrease the number of aggregates. The
523 sample was centrifuged at 1500 × *g* for 5 min at 4°C, and the cell pellet was visible.

524

525 The cells were checked on a hemocytometer by staining with trypan blue (1:1). The
526 approximate number of cells was estimated, and their integrity was investigated. ACME fixed
527 cells were stained with the DNA dye, DRAQ5^{TM}, to sort intact single cells from cellular debris

528 and aggregates (eBioscience 0.66 μL/mL of 5 mM stock). After staining, cells were incubated
529 in the dark and on ice for an hour. The stained cells were sorted using a BD FACSAria Fusion
530 flow cytometer (BD Biosciences) with a red laser (640 nm). In total, 50,000 cells were sorted
531 in collection buffer containing 1X PBS-1% BSA-RNAse inhibitor (40 U/mL) (Fig. S1). The
532 cells were visualized under the far-red channel of a Nikon Ti2 Inverted fluorescence
533 microscope (Fig. S1). The cells were preserved at -20°C by adding DMSO (10% final
534 concentration).
535
536 **sc-RNA-seq via 10X Genomics & sequencing**
537 Frozen cells were thawed on ice and centrifuged at 1500 × g and 4°C. The supernatant was
538 used to wash away the DMSO, followed by adding 1XPBS-1%BSA-RNase inhibitor (40
539 U/mL). Sorted cells were counted on a hemocytometer using trypan blue in a 1:1 ratio and
540 diluted to yield approximately 6000 cells for further processing. The cells underwent
541 centrifugation at 1500 × g at 4°C, then 10X Master Mix was added to the single cells.
542 Subsequently, the cells were loaded onto a 10x Genomics Chromium chip. Gel bead emulsion
543 (GEM) generation, barcoding, reverse transcription, cDNA amplification, and library
544 preparation were carried out according to the 10X Genomics protocol for 3' Gene Expression
545 (v3) user guide (10X Genomics CG000183 Rev C). The target cell recovery rate was set to
546 3000. After the GEM generation, a post-GEM-RT clean-up procedure was performed. cDNA
547 amplification was performed for 16 cycles. The resulting cDNA was analyzed using a Qubit
548 fluorometer and agarose gel electrophoresis. Samples were indexed for library preparation and
549 library concentrations were quantified using KAPA PCR. The combined cDNA libraries were
550 sequenced with a length of 150 bp on an Illumina NovaSeq 6000 sequencing platform at the
551 Australian Genome Research Facility Ltd.
552

553 **Read alignment & cluster analysis**

554 Quality checks of the library were performed using FastQC (Andrews, 2010) (Supplementary
555 Fig. S22). Raw sequencing reads were mapped to the reference *B. diegensis* genome using
556 STARSolo (Kaminow et al., 2021). The genome file of *B. diegensis* (formerly *B. leachii*) was
557 downloaded from the Aniseed Database (http://www.aniseed.cnrs.fr) (Blanchoud et al., 2018).
558 Gene models were identified using the StringTie software (Pertea et al., 2016). First, genome
559 indices were created using STAR 2.7.9 (--genome SAindexNbases 12)(Dobin et al., 2013). The
560 indices were then used to map the raw sequences to the *B. diegensis* genome using STAR 2.7.9,
561 which masks the polyA tail during alignment; therefore, no prior trimming was performed.
562 These run options were selected for the default barcode lengths using a droplet-type algorithm
563 (soloUMIlen 12, soloType Droplet). No barcode read length defined (--
564 soloBarcodeReadLength 0). The empty droplets were then filtered (soloCellFilter
565 EmptyDrops_CR). Finally, sequences with barcodes present within the barcode whitelist were
566 selected while mapping (soloCBwhitelist). The mapping statistics are listed in Table S1.

567

568 After mapping, clustering was performed using Seurat 4.0.1(Stuart et al., 2019) and R 4.1.3.
569 Before clustering, filtering was performed by selecting transcriptomes with 200–2000 genes
570 expressed in at least three cells. The counts were normalized to the total counts using log
571 normalization, and the scale factor was set to 10000. Variability was identified within the 2000
572 genes using the *FindVariableFeatures* function with vst as the selection method. The linear
573 dimensional reduction method was applied to the single-cell transcriptome using principal
574 component analysis. The first 50 PCs for the mature colony were selected based on elbow and
575 jackstraw analyses. Clustering was executed with a 0.8 resolution determined using the clustree
576 R package (Zappia and Oshlack, 2018). The data were plotted using the nonlinear dimensional

577 reduction method and presented using the Uniform Manifold Approximation and Projection
578 (UMAP).
579
580 Differential expression analysis was performed using Seurat package to identify the top genes
581 that were potential markers for each cluster. Top genes were considered significant if Padj <
582 0.05 and had a $\log_2$FC (fold change) value of > 0.5 (Supplementary File 1). Single-cell
583 transcriptomes were saved in the Seurat object, which can be used to check for feature
584 expression. Finally, gene annotation was performed using Metascape (Zhou et al., 2019). The
585 pathway and GO term enrichment were calculated by comparing them to the background genes
586 (all the expressed genes in the dataset with an orthologue, 6039 genes).
587
588 Pseudo-time estimations of single cells were calculated using Monocle 3 (Trapnell et al., 2014),
589 Scanpy 1.10.1 (Wolf et al., 2018), scVelo 0.3.2 (Bergen et al., 2020) and CellRank v. 2.0 (Lange
590 et al., 2022). Code availability: https://github.com/MJWilsonOtago/scRNAseqBotrylloides/ .
591
592 **Probe synthesis, *in situ* hybridization & image acquisition**
593 Probe preparation was initiated by cloning the target genes. Primers were designed to amplify
594 the genes of interest (Table S2). The amplified fragments were inserted into pCRII-TOPO (Life
595 Technologies). Plasmids were sequenced to verify the correct fragment. Digoxygenin (DIG)-
596 labelled sense and antisense probes were synthesized using a 10× DIG RNA labelling mix and
597 SP6/T7 RNA polymerases (Sigma-Aldrich) via *in vitro* transcription. In situ hybridisation was
598 performed as described previously (Zondag et al., 2019). Images were acquired using a Nikon
599 TiE with 60x magnification.
600
601 **Data availability**

The authors declare that all data supporting this study's findings are available in the article and its supplementary information files or through https://megan-wilson-otago.shinyapps.io/Botryllodies_scRNAseq/ .

Acknowledgements

The authors would like to thank the Gemmell Lab of the University of Otago, particularly Joanne Gillum, for their contribution to the single-cell optimization. We also thank Bridget Fellows, Devon Gamble, Justine Gapuz, and Ed Moody for their comments on the final draft. This study was supported by funding from the Department of Anatomy and a University of Otago Research Grant. B.T. was supported by an Anatomy Department Ph.D. scholarship from the University of Otago.

Contributions

B.T.: Data acquisition and interpretation, and manuscript writing. M.M.: funding acquisition, data acquisition, interpretation, and manuscript writing. M.J.W.: Study design, data acquisition and interpretation, funding acquisition, and manuscript writing.

Competing interests

The authors declare no competing interests.

References

Alesci, A., Pergolizzi, S., Lo Cascio, P., Capillo, G., Lauriano, E.R., 2022. Localization of vasoactive intestinal peptide and toll-like receptor 2 immunoreactive cells in endostyle of urochordate Styela plicata (Lesueur, 1823). Microsc Res Tech 85, 2651-2658.

Andrews, S., 2010. FastQC: a quality control tool for high throughput sequence data. Babraham Bioinformatics, Babraham Institute, Cambridge, United Kingdom.

Anselmi, C., Kowarsky, M., Gasparini, F., Caicci, F., Ishizuka, K.J., Palmeri, K.J., Raveh, T., Sinha, R., Neff, N., Quake, S.R., Weissman, I.L., Voskoboynik, A., Manni, L., 2022. Two distinct

630 evolutionary conserved neural degeneration pathways characterized in a colonial chordate.
631 Proceedings of the National Academy of Sciences 119, e2203032119.
632 Bergen, V., Lange, M., Peidli, S., Wolf, F.A., Theis, F.J., 2020. Generalizing RNA velocity to
633 transient cell states through dynamical modeling. Nature biotechnology 38, 1408-1414.
634 Berrill, N.J., 1947a. The developmental cycle of *Botrylloides*. Q J Microsc Sci. 3, 393-407.
635 Berrill, N.J., 1947b. The Developmental Cycle of Botrylloides. Q J Microsc Sci 88, 393-407.
636 Berrill, N.J., 1951. Regeneration and budding in tunicates. Biol Rev 26, 456-475.
637 Blanchoud, S., Rutherford, K., Zondag, L., Gemmell, N.J., Wilson, M.J., 2018. De novo draft
638 assembly of the Botrylloides leachii genome provides further insight into tunicate evolution.
639 Sci Rep 8, 5518.
640 Blanchoud, S., Zondag, L., Lamare, M.D., Wilson, M.J., 2017. Hematological Analysis of the
641 Ascidian Botrylloides leachii (Savigny, 1816) During Whole-Body Regeneration. The Biological
642 bulletin 232, 143-157.
643 Cao, C., Lemaire, L.A., Wang, W., Yoon, P.H., Choi, Y.A., Parsons, L.R., Matese, J.C., Levine, M.,
644 Chen, K., 2019. Comprehensive single-cell transcriptome lineages of a proto-vertebrate.
645 Nature 571, 349-354.
646 Chaudhry, S.S., Cain, S.A., Morgan, A., Dallas, S.L., Shuttleworth, C.A., Kielty, C.M., 2007.
647 Fibrillin-1 regulates the bioavailability of TGFβ1. The Journal of cell biology 176, 355-367.
648 Cima, F., Perin, A., Burighel, P., Ballarin, L., 2001. Morpho-functional characterization of
649 haemocytes of the compound ascidian Botrylloides leachi (Tunicata, Ascidiacea). Acta
650 Zoologica 82, 261-274.
651 Didion, S.P., Ryan, M.J., Didion, L.A., Fegan, P.E., Sigmund, C.D., Faraci, F.M., 2002. Increased
652 superoxide and vascular dysfunction in CuZnSOD-deficient mice. Circ Res 91, 938-944.
653 Dobin, A., Davis, C.A., Schlesinger, F., Drenkow, J., Zaleski, C., Jha, S., Batut, P., Chaisson, M.,
654 Gingeras, T.R., 2013. STAR: ultrafast universal RNA-seq aligner. Bioinformatics 29, 15-21.
655 Ermis Akyuz, E., Bell, S.M., 2022. The Diverse Role of CUB and Sushi Multiple Domains 1
656 (CSMD1) in Human Diseases. Genes (Basel) 13.
657 Fujita, H., Nanba, H., 1971. Fine structure and its functional properties of the endostyle of
658 ascidians, Ciona intestinalis. A part of phylogenetic studies of the thyroid gland. Z Zellforsch
659 Mikrosk Anat 121, 455-469.
660 García-Castro, H., Kenny, N.J., Iglesias, M., Álvarez-Campos, P., Mason, V., Elek, A., Schönauer,
661 A., Sleight, V.A., Neiro, J., Aboobaker, A., 2021. ACME dissociation: a versatile cell fixation-
662 dissociation method for single-cell transcriptomics. Genome biology 22, 1-34.
663 Garcia-Castro, H., Kenny, N.J., Iglesias, M., Alvarez-Campos, P., Mason, V., Elek, A., Schonauer,
664 A., Sleight, V.A., Neiro, J., Aboobaker, A., Permanyer, J., Irimia, M., Sebe-Pedros, A., Solana, J.,
665 2021. ACME dissociation: a versatile cell fixation-dissociation method for single-cell
666 transcriptomics. Genome biology 22, 89.
667 Handford, P., 2000. Fibrillin-1, a calcium binding protein of extracellular matrix. Biochimica et
668 Biophysica Acta (BBA)-Molecular Cell Research 1498, 84-90.
669 Hirano, M., Galarza-Munoz, G., Nagasawa, C., Schott, G., Wang, L., Antonia, A.L., Jain, V., Yu,
670 X., Widen, S.G., Briggs, F.B.S., Gregory, S.G., Ko, D.C., Fagg, W.S., Bradrick, S., Garcia-Blanco,
671 M.A., 2023. The RNA helicase DDX39B activates FOXP3 RNA splicing to control T regulatory
672 cell fate. eLife 12.
673 Hirose, E., Shirae, M., Saito, Y., 2003. Ultrastructures and classification of circulating
674 hemocytes in 9 botryllid ascidians (Chordata: Ascidiacea). Zoological science 20, 647-656.
675 Holland, L.Z., 2016. Tunicates. Current Biology 26, R146-R152.

Holley, M.C., 1986. Cell shape, spatial patterns of cilia, and mucus-net construction in the ascidian endostyle. Tissue Cell 18, 667-684.
Horie, R., Hazbun, A., Chen, K., Cao, C., Levine, M., Horie, T., 2018. Shared evolutionary origin of vertebrate neural crest and cranial placodes. Nature 560, 228-232.
Jiang, A., Zhang, W., Wei, J., Liu, P., Dong, B., 2023. Transcriptional Analysis of the Endostyle Reveals Pharyngeal Organ Functions in Ascidian. Biology (Basel) 12.
Kaminow, B., Yunusov, D., Dobin, A., 2021. STARsolo: accurate, fast and versatile mapping/quantification of single-cell and single-nucleus RNA-seq data. bioRxiv.
Kassmer, S.H., Langenbacher, A.D., De Tomaso, A.W., 2020. Integrin-alpha-6+ Candidate stem cells are responsible for whole body regeneration in the invertebrate chordate Botrylloides diegensis. Nature communications 11, 4435.
Kawamura, K., Sunanaga, T., 2010. Hemoblasts in colonial tunicates: Are they stem cells or tissue-restricted progenitor cells? Development, growth & differentiation 52, 69-76.
Kawamura, K., Tiozzo, S., Manni, L., Sunanaga, T., Burighel, P., De Tomaso, A.W., 2011. Germline cell formation and gonad regeneration in solitary and colonial ascidians. Developmental Dynamics 240, 299-308.
Kharchenko, P.V., Silberstein, L., Scadden, D.T., 2014. Bayesian approach to single-cell differential expression analysis. Nat Methods 11, 740-742.
Kobayashi, H., Tsuneki, K., Akiyoshi, H., Kobayashi, Y., Nozaki, M., Ouji, M., 1983. Histochemical distribution of peroxidase in ascidians with special reference to the endostyle and the branchial sac. Gen Comp Endocrinol 50, 172-187.
Lange, M., Bergen, V., Klein, M., Setty, M., Reuter, B., Bakhti, M., Lickert, H., Ansari, M., Schniering, J., Schiller, H.B., Pe'er, D., Theis, F.J., 2022. CellRank for directed single-cell fate mapping. Nat Methods 19, 159-170.
Langenbacher, A.D., Rodriguez, D., Di Maio, A., De Tomaso, A.W., 2015. Whole-mount fluorescent in situ hybridization staining of the colonial tunicate Botryllus schlosseri. Genesis 53, 194-201.
Manni, L., Burighel, P., 2006. Common and divergent pathways in alternative developmental processes of ascidians. BioEssays : news and reviews in molecular, cellular and developmental biology 28, 902-912.
Manni, L., Zaniolo, G., Cima, F., Burighel, P., Ballarin, L., 2007. Botryllus schlosseri: a model ascidian for the study of asexual reproduction. Developmental dynamics: an official publication of the American Association of Anatomists 236, 335-352.
Meng, X., Chen, M., Su, W., Tao, X., Sun, M., Zou, X., Ying, R., Wei, W., Wang, B., 2018. The differentiation of mesenchymal stem cells to vascular cells regulated by the HMGB1/RAGE axis: its application in cell therapy for transplant arteriosclerosis. Stem Cell Res Ther 9, 85.
Morris, M.E., Rodriguez-Cruz, V., Felmlee, M.A., 2017. SLC and ABC Transporters: Expression, Localization, and Species Differences at the Blood-Brain and the Blood-Cerebrospinal Fluid Barriers. AAPS J 19, 1317-1331.
Mukai, H., Sugimoto, K., Taneda, Y., 1978. Comparative studies on the circulatory system of the compound ascidians, *Botryllus, Botrylloides* and *Symplegma*. Journal of morphology 157, 49-77.
Ojha, H., Ghosh, P., Singh Panwar, H., Shende, R., Gondane, A., Mande, S.C., Sahu, A., 2019. Spatially conserved motifs in complement control protein domains determine functionality in regulators of complement activation-family proteins. Commun Biol 2, 290.

721 Parrinello, D., Sanfratello, M.A., Vizzini, A., Parrinello, N., Cammarata, M., 2015. Ciona
722 intestinalis galectin (CiLgals-a and CiLgals-b) genes are differentially expressed in endostyle
723 zones and challenged by LPS. Fish Shellfish Immunol 42, 171-176.
724 Parrinello, D., Sanfratello, M.A., Vizzini, A., Testasecca, L., Parrinello, N., Cammarata, M., 2017.
725 The Ciona intestinalis immune-related galectin genes (CiLgals-a and CiLgals-b) are expressed
726 by the gastric epithelium. Fish Shellfish Immunol 62, 24-30.
727 Perillo, M., Wang, Y.J., Leach, S.D., Arnone, M.I., 2016. A pancreatic exocrine-like cell
728 regulatory circuit operating in the upper stomach of the sea urchin *Strongylocentrotus*
729 *purpuratus* larva. BMC evolutionary biology 16, 1-15.
730 Pertea, M., Kim, D., Pertea, G.M., Leek, J.T., Salzberg, S.L., 2016. Transcript-level expression
731 analysis of RNA-seq experiments with HISAT, StringTie and Ballgown. Nature protocols 11,
732 1650-1667.
733 Pieknell, K., Sulistio, Y.A., Wulansari, N., Darsono, W.H.W., Chang, M.Y., Ko, J.Y., Chang, J.W.,
734 Kim, M.J., Lee, M.R., Lee, S.A., Lee, H., Lee, G., Jung, B.H., Park, H., Kim, G.H., Kim, D., Cho, G.,
735 Kim, C.H., Ly, D.D., Park, K.S., Lee, S.H., 2022. LIN28A enhances regenerative capacity of human
736 somatic tissue stem cells via metabolic and mitochondrial reprogramming. Cell Death Differ
737 29, 540-555.
738 Reinhardt, D.P., Keene, D.R., Corson, G.M., Pöschl, E., Bächinger, H.P., Gambee, J.E., Sakai, L.Y.,
739 1996. Fibrillin-1: organization in microfibrils and structural properties. Journal of molecular
740 biology 258, 104-116.
741 Ricci, L., Cabrera, F., Lotito, S., Tiozzo, S., 2016. Redeployment of germ layers related TFs shows
742 regionalized expression during two non-embryonic developments. Developmental biology
743 416, 235-248.
744 Rinkevich, B., Ballarin, L., Martinez, P., Somorjai, I., Ben-Hamo, O., Borisenko, I., Berezikov, E.,
745 Ereskovsky, A., Gazave, E., Khnykin, D., 2022. A pan-metazoan concept for adult stem cells: the
746 wobbling Penrose landscape. Biol Rev 97, 299-325.
747 Rinkevich, Y., Douek, J., Haber, O., Rinkevich, B., Reshef, R., 2007. Urochordate whole body
748 regeneration inaugurates a diverse innate immune signaling profile. Developmental biology
749 312, 131-146.
750 Rinkevich, Y., Rosner, A., Rabinowitz, C., Lapidot, Z., Moiseeva, E., Rinkevich, B., 2010. Piwi
751 positive cells that line the vasculature epithelium, underlie whole body regeneration in a basal
752 chordate. Developmental biology 345, 94-104.
753 Rosental, B., Kowarsky, M., Seita, J., Corey, D.M., Ishizuka, K.J., Palmeri, K.J., Chen, S.-Y., Sinha,
754 R., Okamoto, J., Mantalas, G., 2018. Complex mammalian-like haematopoietic system found
755 in a colonial chordate. Nature 564, 425-429.
756 Sasaki, A., Miyamoto, Y., Satou, Y., Satoh, N., Ogasawara, M., 2003. Novel endostyle-specific
757 genes in the ascidian Ciona intestinalis. Zoolog Sci 20, 1025-1030.
758 Sewell, M.T., Legue, E., Liem, K.F., Jr., 2024. Tubb4b is required for multi-ciliogenesis in the
759 mouse. Development 151.
760 Sharma, S., Wang, W., Stolfi, A., 2019. Single-cell transcriptome profiling of the *Ciona* larval
761 brain. Developmental biology 448, 226-236.
762 Stuart, T., Butler, A., Hoffman, P., Hafemeister, C., Papalexi, E., Mauck III, W.M., Hao, Y.,
763 Stoeckius, M., Smibert, P., Satija, R., 2019. Comprehensive integration of single-cell data. Cell
764 177, 1888-1902. e1821.
765 Takagi, W., Sugahara, F., Higuchi, S., Kusakabe, R., Pascual-Anaya, J., Sato, I., Oisi, Y., Ogawa,
766 N., Miyanishi, H., Adachi, N., 2022. Thyroid and endostyle development in cyclostomes
767 provides new insights into the evolutionary history of vertebrates. BMC biology 20, 76.

Takahashi, K., Yamanaka, S., 2006. Induction of pluripotent stem cells from mouse embryonic and adult fibroblast cultures by defined factors. Cell 126, 663-676.
Takahashi, K., Yamanaka, S., 2016. A decade of transcription factor-mediated reprogramming to pluripotency. Nature reviews. Molecular cell biology 17, 183-193.
Temiz, B., Clarke, R.M., Page, M., Lamare, M., Wilson, M.J., 2023. Identification and characterisation of Botrylloides (Styelidae) species from Aotearoa New Zealand coasts. New Zealand Journal of Marine and Freshwater Research, 1-19.
Tiozzo, S., Christiaen, L., Deyts, C., Manni, L., Joly, J.S., Burighel, P., 2005. Embryonic versus blastogenetic development in the compound ascidian Botryllus schlosseri: insights from Pitx expression patterns. Developmental dynamics : an official publication of the American Association of Anatomists 232, 468-478.
Trapnell, C., Cacchiarelli, D., Grimsby, J., Pokharel, P., Li, S., Morse, M., Lennon, N.J., Livak, K.J., Mikkelsen, T.S., Rinn, J.L., 2014. The dynamics and regulators of cell fate decisions are revealed by pseudotemporal ordering of single cells. Nature biotechnology 32, 381-386.
Voskoboynik, A., Soen, Y., Rinkevich, Y., Rosner, A., Ueno, H., Reshef, R., Ishizuka, K.J., Palmeri, K.J., Moiseeva, E., Rinkevich, B., 2008a. Identification of the endostyle as a stem cell niche in a colonial chordate. Cell stem cell 3, 456-464.
Voskoboynik, A., Soen, Y., Rinkevich, Y., Rosner, A., Ueno, H., Reshef, R., Ishizuka, K.J., Palmeri, K.J., Moiseeva, E., Rinkevich, B., Weissman, I.L., 2008b. Identification of the endostyle as a stem cell niche in a colonial chordate. Cell stem cell 3, 456-464.
Wagner, T., Beer, L., Gschwandtner, M., Eckhart, L., Kalinina, P., Laggner, M., Ellinger, A., Gruber, R., Kuchler, U., Golabi, B., Tschachler, E., Mildner, M., 2019. The Differentiation-Associated Keratinocyte Protein Cornifelin Contributes to Cell-Cell Adhesion of Epidermal and Mucosal Keratinocytes. The Journal of investigative dermatology 139, 2292-2301 e2299.
Wolf, F.A., Angerer, P., Theis, F.J., 2018. SCANPY: large-scale single-cell gene expression data analysis. Genome biology 19, 15.
Wright, R.K., Ermak, T.H., 1982. Cellular defense systems of the Protochordata, Phylogeny and Ontogeny. Springer, pp. 283-320.
Wu, K., Ahmad, T., Eri, R., 2022. LIN28A: A multifunctional versatile molecule with future therapeutic potential. World J Biol Chem 13, 35-46.
Yamagishi, M., Huang, T., Hozumi, A., Onuma, T.A., Sasakura, Y., Ogasawara, M., 2022. Differentiation of endostyle cells by Nkx2-1 and FoxE in the ascidian Ciona intestinalis type A: insights into shared gene regulation in glandular- and thyroid-equivalent elements of the chordate endostyle. Cell Tissue Res 390, 189-205.
Zappia, L., Oshlack, A., 2018. Clustering trees: a visualization for evaluating clusterings at multiple resolutions. Gigascience 7, giy083.
Zhang, L., Yang, Y., Li, B., Scott, I.C., Lou, X., 2018. The DEAD-box RNA helicase Ddx39ab is essential for myocyte and lens development in zebrafish. Development 145.
Zhang, T., Xu, Y., Imai, K., Fei, T., Wang, G., Dong, B., Yu, T., Satou, Y., Shi, W., Bao, Z., 2020. A single-cell analysis of the molecular lineage of chordate embryogenesis. Science advances 6, eabc4773.
Zhou, Y., Zhou, B., Pache, L., Chang, M., Khodabakhshi, A.H., Tanaseichuk, O., Benner, C., Chanda, S.K., 2019. Metascape provides a biologist-oriented resource for the analysis of systems-level datasets. Nature communications 10, 1-10.
Zondag, L., Clarke, R.M., Wilson, M.J., 2019. Histone deacetylase activity is required for Botrylloides leachii whole-body regeneration. J Exp Biol 222.